HAL

open science

Dissolution Anisotropy of Pyroxenes: A Surrogate Model for Steady-State Enstatite Dissolution Resulting from Stochastic Simulations of the Hydrolysis Process

Arnaud Bouissonnié, Damien Daval, Philippe Ackerer

▶ **To cite this version:**

HAL Id: hal-03010626
https://hal.science/hal-03010626

Submitted on 17 Nov 2020

1   # The Dissolution Anisotropy of Pyroxenes: A Surrogate Model for

2   # Steady-State Enstatite Dissolution Resulting From Stochastic

3   # Simulations of the Hydrolysis Process

4

5   Arnaud Bouissonnié[1,*], Damien Daval[1], Philippe Ackerer[1]

6

7   [1] Université de Strasbourg – CNRS / ENGEES – EOST, Laboratoire d'Hydrologie et de

8   Géochimie de Strasbourg, 1 Rue Blessig, 67084 Strasbourg, France

9

10 [*]corresponding author: arnaud.bouissonnie@etu.unistra.fr (A. Bouissonnié)

11 Tel: +33 (0)3 68 85 05 47; Fax: +33(0)3 68 85 04 02

12

13

14

15

16

17

18

19

20

21

22

23

24

Abstract

Over the past decades, the field of mineral dissolution kinetics has undergone a spectacular evolution, with an increasingly detailed description of the atomic scale mechanisms of fluid-solid interactions. The development of probabilistic dissolution models has played a prominent role in this evolution, as they allow for bridging the outputs of *ab initio* calculations to macroscopic observables such as dissolution rates and nanoscale surface features. It is however admitted that these models cannot be easily adapted to simulate natural systems at large space and time scales due to the restricted dimensions and durations that can be simulated numerically. In the present study, we demonstrate that the steady-state outputs of the face-specific stochastic treatment of enstatite dissolution, which was experimentally validated in a previous paper, can be boiled down to a single analytical expression under the form:

$$r_{bulk}^{(hkl)} = k P_{Mg-O-Mg}^{\alpha} P_{Mg-O-Si}^{\beta} P_{Si-O-Si}^{\gamma}$$

where $r_{bulk}^{(hkl)}$ is the steady-state dissolution rate of a defect-free (*hkl*) face [Å/iter], $P_{M-O-M'}$ stands for the bond-breaking probability of the M-O-M' bond, and k, α, β and γ are fitting parameters adjusted following the outputs of the stochastic simulations. When dislocations outcrop at the surface of a given (*hkl*) face of enstatite, the relation then becomes:

$$r^{(hkl)} = r_{bulk}^{(hkl)} + r_{dislocation}^{(hkl)} \left(P_{Mg-O-Mg}, P_{Mg-O-Si}, P_{Si-O-Si} \right)$$

where $r_{dislocation}^{(hkl)}$ stands for the contribution of the dislocations to the overall dissolution rate. The derivation of simple analytical expressions to get steady-state rate data that are similar to those obtained using stochastic dissolution models, may contribute to parametrize efficiently the bond-breaking probability of various atoms for pyroxene solid solutions, and raises the question of the extension of such surrogate expressions to other silicate structures. Finally, the

48   development of surrogate models such as those reported here represents one of the possible

49   strategies for upscaling dissolution processes from the atomic scale to the micron scale.

1. Introduction

Many complementary approaches have been developed to predict the fate of water-rock interactions, at various space and time scales. Historically, the conceptual framework underpinning the corresponding models has been closely linked to the disciplinary field in which they were developed.

When dealing with the Earth system, the first attempts to develop weathering rate laws for large space (km²) and time (Myr) scales were undoubtedly phenomenological, and strongly relied on empirical relations. The pioneering work of Berner and coworkers, aimed at reconstructing the evolution of the CO_2 concentration in the atmosphere during the Phanerozoic through the development of the BLAG [1] and GEOCARB [2-4] codes, was based on model weathering reactions, whose rates were largely parametrized according to empirical rate-runoff, rate-pCO_2 and rate-temperature relations inferred from field measurements. Since the early 90s, this approach has been gradually superseded by reactive transport models, where the source-terms of the classical reaction-dispersion-advection equation are described following kinetic rate laws derived from dissolution experiments conducted on powdered single-crystals. Although the corresponding rate equations, which relate the dissolution rate to fundamental parameters such as temperature, pH, surface area or solution saturation state, were originally claimed to result from the transition state theory (TST) [5-7], several studies subsequently questioned the theoretical validity of the extension of TST to silicate dissolution [8-9], the experimental validation of which being described as nothing more than a fitting exercise with little physical basis by some authors [10]. More generally, a growing number of experimental studies have underlined the limitations of TST-based relations, which fail to accurately relate dissolution rates to solution saturation state [11-19], and are unable to account for the variability (heterogeneity and anisotropy) of crystal dissolution rates [20-28]. With respect to the relation between dissolution rate and fluid saturation state, the deviation from a TST-

75 behavior has often been attributed to the nucleation and opening of etch pits where

76 dislocations outcrop at the mineral's surface [11, 19, 23, 29-32]. Etch pits have been extensively

77 reported for a wide variety of minerals [22-23, 32-38], when the fluid under saturation is large

78 enough and does not exceed a critical value of the Gibbs free energy. The efficiency of these

79 sites to enhance mineral dissolution rate has been showed both experimentally and

80 numerically, and is accounted for by the stepwave model [31]. At the atomic-scale, the opening

81 of etch pits results in an increase of the density of kink and step sites. This process exposes

82 atoms with a lower coordination to the fluid which are, as a result, more rapidly dissolved.

83 More generally, the reactivity of minerals is highly heterogeneous, with hotspots of reactivity

84 such as kinks, steps (and ultimately crystal edges and corners) and can be accurately captured

85 by the "rate spectra" concept [20, 39]. Finally, several studies have pointed out that mineral

86 dissolution is anisotropic [19, 22-23, 38, 40-41], resulting from the anisotropic distribution of atomic

87 positions in the crystal lattice. These observations have emphasized the need for deeper

88 experimental and theoretical studies of fluid-mineral interactions from the atomic- to the nm-

89 scale to unravel the dissolution mechanisms.

90   Precisely at the other end of the spatiotemporal spectrum, the advent of microscopic

91 and spectroscopic techniques of characterization of the fluid-mineral interface offered new

92 avenues to understand mineral reactivity [26, 42-53]. Studies dedicated to the molecular-scale

93 description of the silicate dissolution process following *ab initio* quantum mechanical

94 calculations and molecular dynamics (MD) models emerged some 20 years ago [54-59]. These

95 studies provided essential theoretical insights into the dissolution process. Admittedly, the

96 corresponding studies have been of limited direct interest (and were not intended) to model

97 chemical weathering in natural settings, due to the restricted durations and dimensions of the

98 system that can be simulated numerically.

A first intermediate step in the upscaling process of dissolution reaction rates has been successfully reached with the emergence of stochastic models of silicate and carbonate dissolution [25, 28, 36, 48, 53, 57, 60-69], whose parametrization may strongly rely on the results of *ab initio* calculations mentioned above, with considerable simplifications of the reaction details. Such an approach dramatically increased the size of the studied systems from clusters of a few atoms to nanocrystals of several tens of millions of atoms, simulating time scales of up to several weeks [41, 70]. However, implementing such models into reactive transport codes is not an easy task since they usually do not provide the rate laws that are required by these codes to predict the rates of water-rock interactions at large space and time scales [71-72]. Promising strategies combining Monte Carlo simulations and Voronoi methods have been recently developed to circumvent this issue [39, 73], offering the perspective to reach the next step in the upscaling process, i.e., the continuum scale, where reactive transport can be applied. Such recent breakthroughs emphasize the crucial importance of maintaining efforts to investigate into more details the various theoretical and empirical emerging relations of stochastic dissolution models, which represents one of the goals of the present paper.

In a previous study [41], we developed a probabilistic model of enstatite dissolution which successfully reproduced the measured anisotropy of enstatite dissolution rates and associated surface features. In the present study, hundreds of simulations were conducted with this model by varying the bond-breaking probabilities of the crystal to explore the analytical relation that may link together the detachment of individual atoms from the enstatite surface to the overall face-specific dissolution rates. This work was in part motivated by the fact that mineral dissolution kinetics is often treated by mixing macroscopic parameters with microscopic ones, resulting in rate laws for which the theoretical basis remains questionable (see discussion in e.g. [9]). Here we illustrate how overall rate constants may be derived from atomic-scale parameters, considering especially the bond-breaking probability of hydrolysis

124 processes. In particular, we show that, at steady-state conditions, an analytical relation can be

125 derived to express the overall dissolution rate constant, whose parameters can be adjusted

126 following the outputs of numerical simulations performed at the atomic scale. We then show

127 that the resulting analytical relation can be used to predict the steady-state enstatite face-

128 specific dissolution rates over a wide range of bond-breaking probabilities. This relation is

129 then further extended from defect-free surfaces to defective surfaces impacted by screw

130 dislocations. Finally, we discuss the implications of such surrogate expressions, both from the

131 perspective of the mechanisms of pyroxene dissolution and for the upscaling of silicate

132 dissolution rates.

133

134 2. Methods

135 *2.1 Model description and algorithms*

136 A complete description of the model is given in Bouissonnié et al. [41]. In short, the

137 positions of Mg, Si and O atoms provided by Hugh-Jones and Angel [74] are used to create the

138 enstatite cell thanks to the symmetry elements of the *Pbca* space group. Mg and Si atoms are

139 then linked to the 6 and 4 nearest O atoms respectively. Since probabilistic dissolution models

140 generally consider the bond-breaking probabilities of M-O-M' bonds [30, 36, 69], each Mg and Si

141 atom is connected to its first coordination sphere [36].

142 Usually, the probability attributed with one event (i.e. the bond-breaking probability)

143 is written as follows [30]:

$$P = e^{\frac{-E_a}{k_B T}} \tag{1}$$

144 where P stands for the bond-breaking probability, E_a for the activation energy of the bond

145 hydrolysis (J), k_B for the Boltzmann constant (J/K) and T for the temperature (K). In the

146 present study, the most likely bond-breaking probability (i.e., the bond hydrolysis associated

147   ~~to~~ with the lowest activation energy, Mg-O-Mg) was arbitrarily set to 0.99 and the two other

148   probabilities were scaled according to the differences between their corresponding activation

149   energies following:

$$\frac{P_A}{P_B} = e^{-\frac{(E_a^A - E_a^B)}{k_B T}} \tag{2}$$

150   where A and B represent two different bonds.

151   In agreement with previous studies [48, 61-66], an "all-or-none" approach has been used.

152   This approach considers the hydrolysis of atoms instead of individual bonds. In other words,

153   for a given simulated step, an atom is released only when all the remaining bonds that connect

154   the atom to the surface of the crystal are broken simultaneously. Otherwise, the corresponding

155   atom remains connected to the surface. The probability of an atom M to be released in the

156   fluid depends on the number and type of atomic bonds present in its first coordination sphere.

157   In the case of the enstatite, this probability can be written as follows:

$$P_M = e^{-n\frac{E_{M-O-Mg}}{k_B T}} e^{-m\frac{E_{M-O-Si}}{k_B T}} = P_{M-O-Mg}^n P_{M-O-Si}^m \tag{3}$$

158   where n and m stand for the number of bonds that the considered atom shares with Mg and Si

159   atoms respectively.

160   The dissolution algorithm was described in details in Bouissonnié et al. [41] and is

161   schematically represented in Fig. 1. Such algorithms have previously proven successful to

162   simulate the dissolution of silicate materials (e.g. [41, 48, 61]). In short, a random number Z

163   uniformly distributed between 0 and 1 is drawn for each atom at the surface defined by an

164   incomplete coordination sphere (i.e. an atom at the crystal surface). If $Z < P_M$, all atomic

165   bounds are broken and the atom is considered as dissolved (removed from the surface); if not,

166   the atom stays at the surface. The first coordination spheres of the remaining atoms are then

167   updated if necessary (i.e., when a removed atom was belonging to the coordination spheres of

168   one of the neighboring remaining atoms). Because coordination spheres are modified, the

169 probability of dissolution P_M of the corresponding atoms increases. In such kinds of

170 algorithms, each iteration step corresponds to a given simulated duration, and the time-step is

171 therefore constant for all simulations. The proportionality factor to convert the number of

172 iterations into time is not known a priori, and can be determined by comparing the outputs of

173 a simulation with experimental data (see [41] for details). This aspect contrasts with kinetic

174 Monte Carlo algorithms based on a "divide and conquer" approach [36, 63], which use an

175 adaptive time step that varies at each iteration as a function of the random number that is

176 drawn, corresponding to a specific surface site that is dissolved during the iteration. The main

177 strengths of the "divide and conquer" approach are that they allow for a direct link between

178 time and the number of iterations, while precluding the existence of "dead" iterations,

179 reducing accordingly the computing time required to simulate a given process. Conversely,

180 "dead" iterations may sometimes occur over the course of the algorithm that we used

181 (essentially, at the beginning of the simulations), but as opposed to the "divide and conquer"

182 approach, it allows for simultaneous events to occur over a given iteration (and time step).

183 Although both methods should ultimately provide identical results (see theoretical derivation

184 in [75]), to the best of our knowledge, a comparison between both types of algorithms has never

185 been proposed for mineral dissolution, and is out of the scope of the present study.

186   The impact of dislocation density has also been studied by running additional

187 simulations for the (100) face. Dislocations were introduced as lines running parallel to the

188 [100] axis, in agreement with previous observations [76]. To simulate the faster dissolution at

189 dislocation sites (placed at the center of the reactive surface), the bond-breaking probabilities

190 associated to with the atoms belonging to the dislocation line were set to 1 following

191 Kurganskaya and LuttgeKurganskaya and Luttge [36].

192   One of the goals of this study was to understand how the dissolution rate evolves as a

193   function of the probabilities used as input parameters. To perform this sensitivity analysis,

194   each of the three fundamental probabilities ($P_{Mg-O-Mg}$, $P_{Si-O-Mg}$, or $P_{Si-O-Si}$) was sampled in a

195   given range while the other two remained constant.
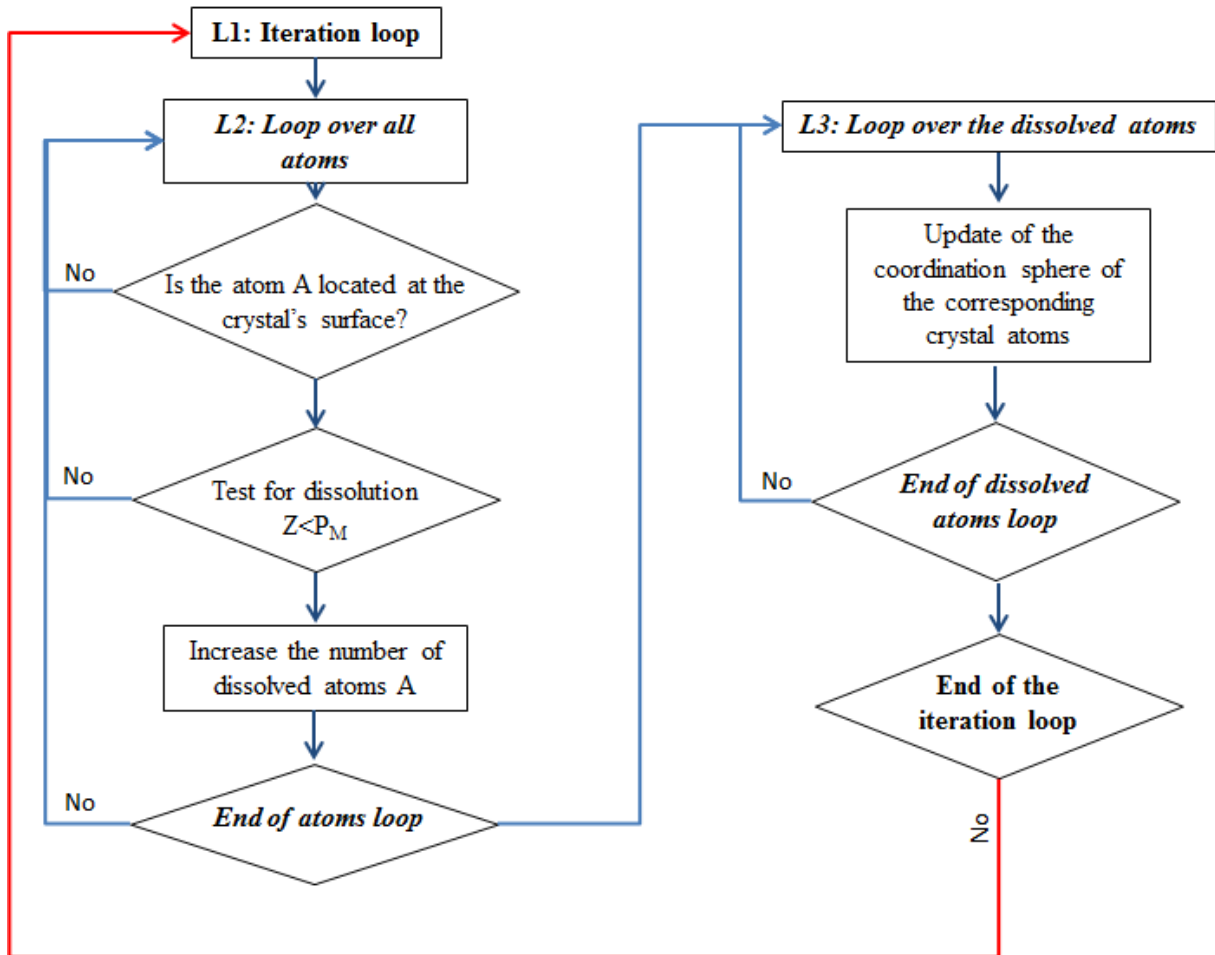
Figure 1 Scheme of the numerical algorithm of the probabilistic model.

196   Finally, the boundary conditions (BC) were set as follows: atoms that are part of the

197   sides of the simulated volume cannot be dissolved. Since it can induce a dependence of the

198   dissolution rate on the dimensions of the simulated surface, we verified that the simulated

199   surface area was large enough to avoid any impact of the BC on the dissolution rate.

200

201   *2.2. Outputs of the model*

202   In order to determine the dissolution rate, the number of released Mg and Si atoms is

203   stored at each step (iteration). In this study, the dissolution rate calculation is based on the

204   release of Si atoms (equivalent to the one based on Mg atoms departure and mean surface

205   height at steady-state conditions [41]):

$$r^{(hkl)} = \frac{V_{cell}}{iter \times N_{Si,cell} \times S} \sum_{i=1}^{iter} N_{Si,i} \qquad (4)$$

206   where $r^{(hkl)}$ stands for the dissolution rate (Å/it) of a given face (here, either (100), (010) or

207   (001)), $N_{Si,i}$ for the number of Si atoms released at each iteration i, $N_{Si,cell}$ for the number of Si

208   atoms in enstatite cell (16), $iter$ for the total number of iterations, and S for the geometric

209   surface area of the crystal face (Å²). The second output of the model is related to the chemical

210   environment of the atoms when they are released from the surface. In particular, knowledge

211   of the first coordination sphere of each atom that has been dissolved allows for the

212   determination of the number of Mg and Si atoms that were connected to the released M

213   atoms. As opposed to other similar numerical studies (e.g. [77-78]), our study was not aimed to

214   capture the intrinsic heterogeneous distribution of reaction rates at the simulated crystal

215   surface. Instead, our primary goal was to provide an analytical expression for the overall face-

216   specific steady state dissolution rate as a function of bond-breaking probabilities, which has to

217   be achieved at the scale of a given face, echoing the face-specific dissolution rates frequently

218   reported from dissolution experiments (see [39, 79] for an overview).

219

3. Results

221   *3.1. Dissolution rate evolution as a function of bond-breaking probabilities*

222
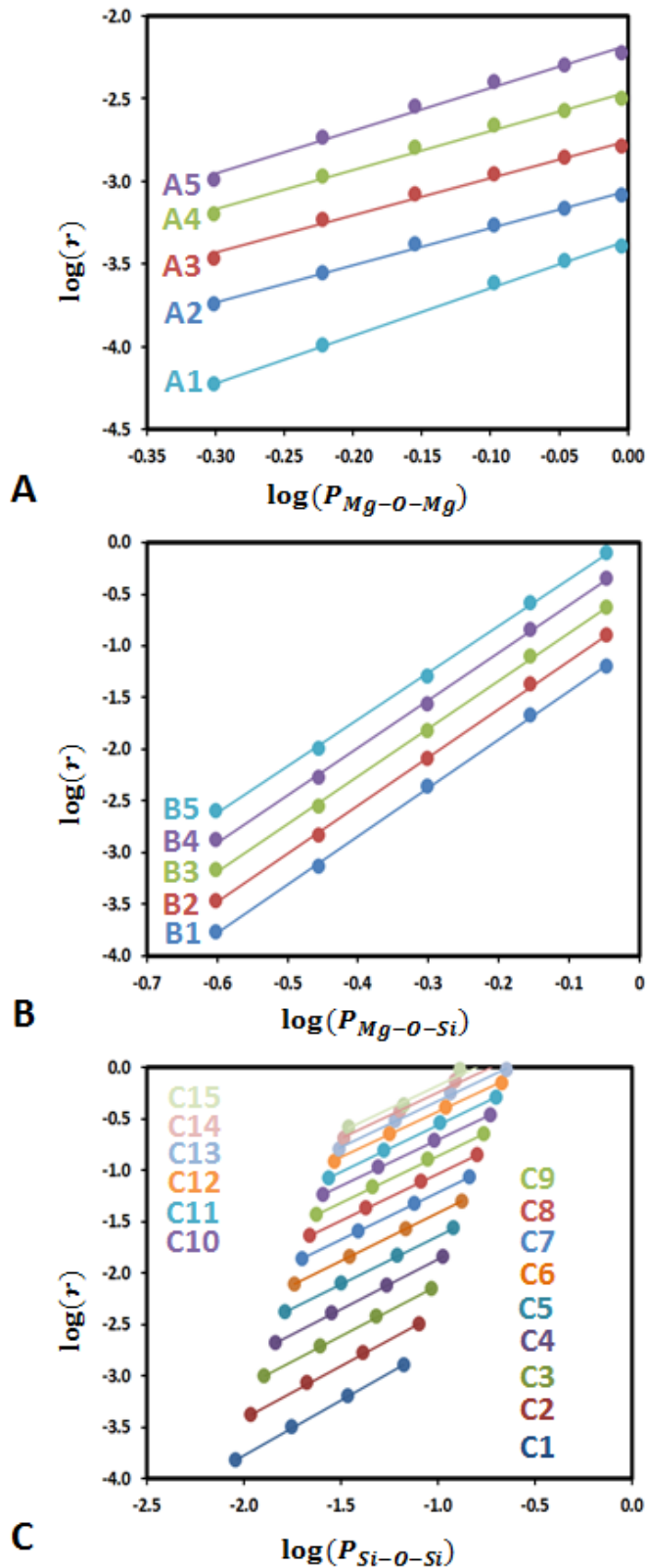
Fig.2. Results of the different simulations for the (100) face. Each graph represents the evolution of the steady-state dissolution rate as a function of the logarithm of: (A) $P_{Mg\text{-}O\text{-}Mg}$, (B) $P_{Mg\text{-}O\text{-}Si}$ and (C) $P_{Si\text{-}O\text{-}Si}$. Each color represents a different ΔEa between the two other probabilities which remains fixed. Slopes and intercepts are listed in Table 1. Legends correspond to the code indicated for each group of simulations. These codes are used in Table 1 to indicate which simulation corresponds to which groups of data.

223

	$P_{Mg-O-Mg}$	$P_{Mg-O-Si}$	$P_{Si-O-Si}$	ΔE (Mg-O-Mg-Mg-O-Si) (kJ/mol)	ΔE (Mg-O-Si-Si-O-Si) (kJ/mol)	ΔE (Mg-O-Mg-Si-O-Si) (kJ/mol)	a	b	R^2	Fig 2 code
	0.99 - 0.50	0.30	0.01	-	10.0	-	2.87	-3.36	1.00	A1
	0.99 - 0.60	0.30	0.02	-	8.0	-	2.23	-3.06	1.00	A2
	0.99 - 0.70	0.30	0.04	-	6.0	-	2.26	-2.75	0.99	A3
	0.99 - 0.80	0.30	0.08	-	4.0	-	2.37	-2.46	0.99	A4
	0.99 - 0.90	0.30	0.15	-	2.0	-	2.59	-2.18	0.99	A5
	0.99	0.90 - 0.25	0.01	-	-	14.0	4.68	-0.97	1.00	B1
	0.99	0.90 - 0.26	0.02	-	-	12.0	4.67	-0.68	1.00	B2
(100)	0.99	0.90 - 0.27	0.04	-	-	10.0	4.62	-0.41	1.00	B3
	0.99	0.90 - 0.28	0.07	-	-	8.0	4.59	-0.15	1.00	B4
	0.99	0.90 - 0.29	0.14	-	-	6.0	4.53	0.10	1.00	B5
	0.99	0.25	0.0665 - 0.0091	4.2	-	-	1.06	-1.64	1.00	C1
	0.99	0.30	0.0798 - 0.0109	3.6	-	-	1.02	-1.37	1.00	C2
	0.99	0.35	0.0930 - 0.0128	3.1	-	-	0.98	-1.14	1.00	C3
	0.99	0.40	0.1063- 0.0146	2.7	-	-	0.97	-0.90	1.00	C4

0.99	0.45	0.1196 - 0.0164	2.4	-	-	0.94	-0.70	1.00	C5
0.99	0.50	0.1329 - 0.0182	2.1	-	-	0.93	-0.49	1.00	C6
0.99	0.55	0.1462 - 0.2000	1.8	-	-	0.92	-0.29	1.00	C7
0.99	0.60	0.1595 - 0.0219	1.5	-	-	0.92	-0.12	1.00	C8
0.99	0.65	0.1728 - 0.0237	1.3	-	-	0.91	0.05	1.00	C9
0.99	0.70	0.1861 - 0.0255	1.0	-	-	0.90	0.20	1.00	C10
0.99	0.75	0.1994 - 0.0273	8.4	-	-	0.90	0.34	1.00	C11
0.99	0.80	0.2127 - 0.0292	6.4	-	-	0.89	0.45	1.00	C12
0.99	0.85	0.2260 - 0.0310	4.6	-	-	0.90	0.57	1.00	C13
0.99	0.90	0.2393 - 0.0328	2.9	-	-	0.90	0.66	1.00	C14
0.99	0.95	0.2526 - 0.0346	1.2	-	-	0.89	0.72	0.99	C15

	$P_{Mg-O-Mg}$	$P_{Mg-O-Si}$	$P_{Si-O-Si}$	ΔE (Mg-O-Mg-Mg-O-Si) (kJ/mol)	ΔE (Mg-O-Si-Si-O-Si) (kJ/mol)	ΔE (Mg-O-Mg-Si-O-Si) (kJ/mol)	a	b	R^2
	0.99 - 0.50	0.30	0.01	-	10.0	-	2.18	-3.08	1.00
	0.99 - 0.60	0.30	0.02	-	8.0	-	2.24	-2.83	1.00
	0.99 - 0.70	0.30	0.04	-	6.0	-	2.24	-2.60	1.00
	0.99 - 0.80	0.30	0.08	-	4.0	-	2.21	-2.39	1.00
	0.99 - 0.90	0.30	0.15	-	2.0	-	2.21	-2.18	1.00
	0.99	0.90 - 0.25	0.01	-	-	14.0	4.48	-0.78	1.00
(010)	0.99	0.90 - 0.26	0.02	-	-	12.0	4.48	-0.54	1.00
	0.99	0.90 - 0.27	0.04	-	-	10.0	4.72	-0.19	1.00
	0.99	0.90 - 0.28	0.07	-	-	8.0	4.79	0.72	1.00
	0.99	0.90 - 0.29	0.14	-	-	6.0	4.79	0.29	1.00
	0.99	0.25	0.0665 -0.0091	4.2	-	-	0.75	-1.92	1.00
	0.99	0.30	0.0798 - 0.0109	3.6	-	-	0.82	-1.48	1.00
	0.99	0.35	0.0930 - 0.0128	3.1	-	-	0.75	-1.23	1.00

0.99	0.40	0.1063- 0.0146	2.7	-	-	0.76	-0.94	1.00
0.99	0.45	0.1196 - 0.0164	2.4	-	-	0.77	-0.68	1.00
0.99	0.50	0.1329 - 0.0182	2.1	-	-	0.79	-0.45	1.00
0.99	0.55	0.1462 - 0.2000	1.8	-	-	0.79	-0.25	1.00
0.99	0.60	0.1595 - 0.0219	1.5	-	-	0.79	-0.06	1.00
0.99	0.65	0.1728 - 0.0237	1.3	-	-	0.78	0.10	1.00
0.99	0.70	0.1861 - 0.0255	1.0	-	-	0.78	0.25	1.00
0.99	0.75	0.1994 - 0.0273	8.4	-	-	0.77	0.38	0.99
0.99	0.80	0.2127 - 0.0292	6.4	-	-	0.74	0.47	0.99
0.99	0.85	0.2260 - 0.0310	4.6	-	-	0.71	0.54	0.98
0.99	0.90	0.2393 - 0.0328	2.9	-	-	0.66	0.59	0.97
0.99	0.95	0.2526 - 0.0346	1.2	-	-	0.60	0.60	0.94

	$P_{Mg-O-Mg}$	$P_{Mg-O-Si}$	$P_{Si-O-Si}$	ΔE (Mg-O-Mg-Mg-O-Si) (kJ/mol)	ΔE (Mg-O-Si-Si-O-Si) (kJ/mol)	ΔE (Mg-O-Mg-Si-O-Si) (kJ/mol)	a	b	R^2
	0.99 - 0.50	0.30	0.01	-	10.0	-	7.46	-1.72	1.00
	0.99 - 0.60	0.30	0.02	-	8.0	-	6.77	-1.77	1.00
	0.99 - 0.70	0.30	0.04	-	6.0	-	6.64	-1.73	0.99
	0.99 - 0.80	0.30	0.08	-	4.0	-	5.88	-1.74	0.98
	0.99 - 0.90	0.30	0.15	-	2.0	-	5.05	-1.73	0.96
	0.99	0.90 - 0.25	0.01	-	-	14.0	4.09	0.39	1.00
(001)	0.99	0.90 - 0.26	0.02	-	-	12.0	4.20	0.46	1.00
	0.99	0.90 - 0.27	0.04	-	-	10.0	4.23	0.48	1.00
	0.99	0.90 - 0.28	0.07	-	-	8.0	4.21	0.49	1.00
	0.99	0.90 - 0.29	0.14	-	-	6.0	4.23	0.51	1.00
	0.99	0.25	0.0665 -0.0091	4.2	-	-	0.17	-1.81	0.99
	0.99	0.30	0.0798 - 0.0109	3.6	-	-	0.15	-1.52	0.97
	0.99	0.35	0.0930 - 0.0128	3.1	-	-	0.13	-1.27	0.98

0.99	0.40	0.1063- 0.0146	2.7	-	-	0.12	-1.04	0.99
0.99	0.45	0.1196 - 0.0164	2.4	-	-	0.15	-0.80	0.99
0.99	0.50	0.1329 - 0.0182	2.1	-	-	0.12	-0.63	0.99
0.99	0.55	0.1462 - 0.2000	1.8	-	-	0.12	-0.45	0.99
0.99	0.60	0.1595 - 0.0219	1.5	-	-	0.11	-0.30	0.99
0.99	0.65	0.1728 - 0.0237	1.3	-	-	0.12	-0.14	1.00
0.99	0.70	0.1861 - 0.0255	1.0	-	-	0.14	0.02	1.00
0.99	0.75	0.1994 - 0.0273	8.4	-	-	0.14	0.14	0.99
0.99	0.80	0.2127 - 0.0292	6.4	-	-	0.14	0.26	0.99
0.99	0.85	0.2260 - 0.0310	4.6	-	-	0.14	0.35	0.98
0.99	0.90	0.2393 - 0.0328	2.9	-	-	0.15	0.44	0.98
0.99	0.95	0.2526 - 0.0346	1.2	-	-	0.16	0.51	0.95

Table 1. Different ΔE_a values used in this study (the "-" symbol indicates that ΔE_a varies). The slope (a), intercept (b) and correlation coefficient (R^2) of the linear regression of $\log(r) = f(\log(P))$ are given in the last three columns (see text for details). When $P_{Mg-O-Mg}$ was left constant, its value was set to 0.99. This value allows for minimizing the simulation time required while having the possibility to associate a corresponding physical ΔE_a value. When the relation between dissolution rate and $P_{Mg-O-Mg}$ was studied, $P_{Mg-O-Si}$ was arbitrarily set to 0.3. Finally, the chosen probabilities were constrained by $P_{Mg-O-Mg} > P_{Mg-O-Si} > P_{Si-O-Si}$.

In total, 345 simulations have been conducted (115 per face) to explore a wide range

of activation energies. Over these 115 simulations, 30 were dedicated to unravelling the

dependence of the dissolution rate evolution on $P_{Mg-O-Mg}$, 25 on $P_{Mg-O-Si}$, and 60 on $P_{Si-O-Si}$.
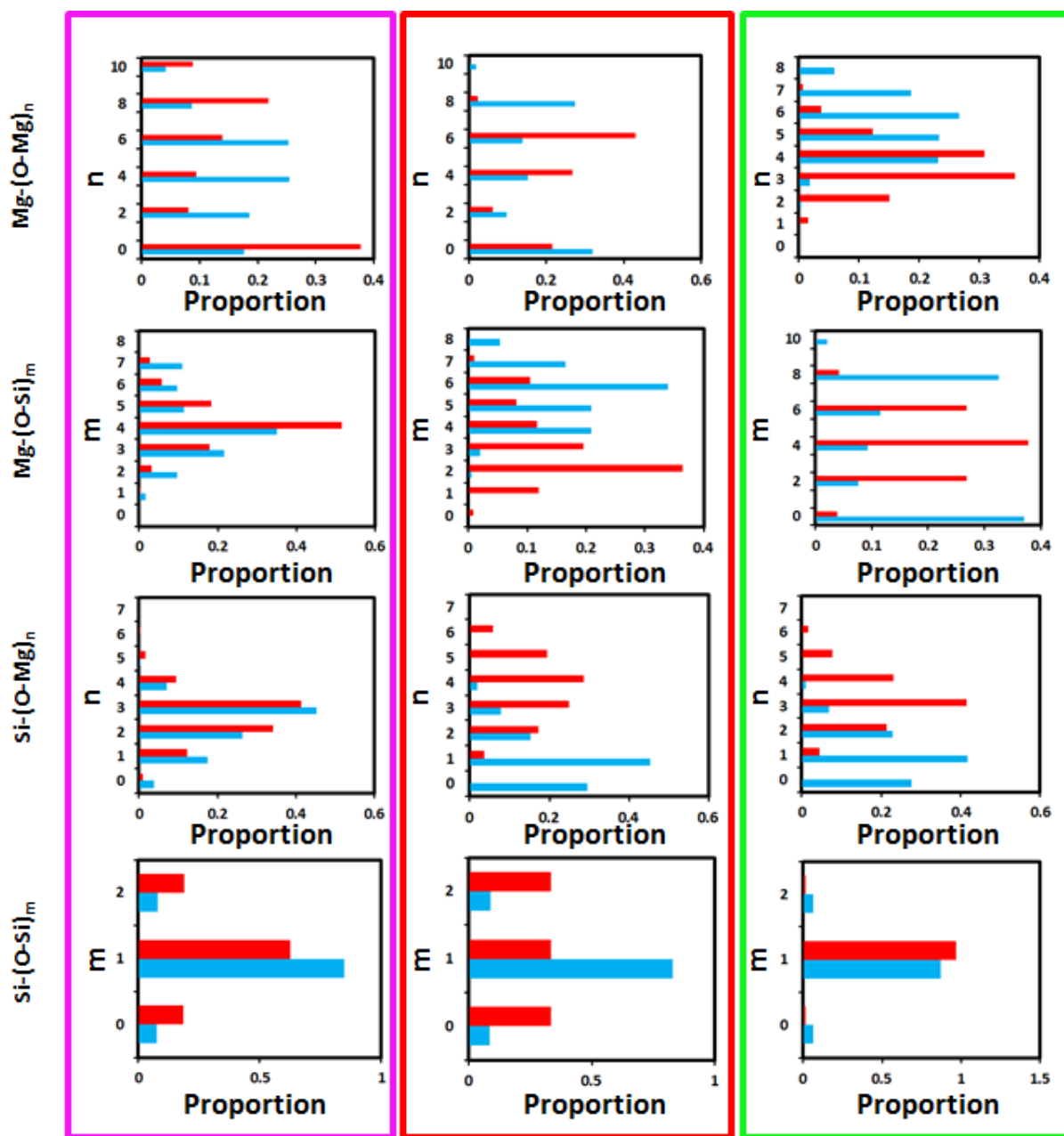

Fig.3. Distribution of the different coordination spheres of an atom right before its dissolution. The first two lines depict Mg atoms, and the following two lines, Si. The proportion is defined by the number of atoms at the surface having m or n bounds divided by the total number of atoms, so that the sum of all modes is 1. Blue and red bars correspond to a set of low ($P_{Mg-O-Mg} = 0.5$, $P_{Mg-O-Si} = 0.3$ and $P_{Si-O-Si} = 0.0109$) and high ($P_{Mg-O-Mg} = 0.99$, $P_{Mg-O-Si} = 0.3$ and $P_{Si-O-Si} = 0.1547$) probability values, respectively. Magenta, red and green rectangle stand for the simulations on (100), (010) and (001) faces respectively.

227 As an illustration, the treatment of the outputs of the simulation conducted with the (100) face

228 is depicted in Fig. 2. As expected, the simulations with the lowest probabilities correspond to

229 those resulting in the lowest steady-state dissolution rates. The different datasets of

230 probabilities (one set corresponds to one value of $P_{Mg\text{-}O\text{-}Mg}$, $P_{Mg\text{-}O\text{-}Si}$ and $P_{Si\text{-}O\text{-}Si}$ as the master

231 variable, all else being constant) have been sorted into different groups according to their

232 fixed ΔEa value. A total of 25 groups per face were analyzed (5 groups of 6 datasets, 5 groups

233 of 5 datasets and 15 groups of 4 datasets for the $r = f(P_{Mg-O-Mg})$, $r = f(P_{Mg-O-Si})$ and

234 $r = f(P_{Si-O-Si})$ cases respectively). These different groups and the full dataset are listed in

235 the Table 1.

236 A linear relationship between the logarithm of the dissolution rate and the logarithm of

237 the bond-breaking probabilities can be observed for the different simulations (see Fig. 2). This

238 linear model matches results from numerical simulations quite satisfactorily. Moreover, the

239 slope remains constant when changing the activation energy for the hydrolysis of one bond,

240 whatever the difference in the activation energy of the two other bonds (i.e. the slopes are the

241 same for the results shown in each Fig. 2A, 2B and 2C). Slopes, intercepts and R^2 of these

242 linear regressions are listed in Table. 1.

243

244 *3.2. Mean first coordination sphere of released atoms*

245 The attainment of a mean surface configuration when steady-state dissolution rates are

246 reached represents a common trait of all simulations. The corresponding mean first

247 coordination spheres of the M atoms at the iteration step of their detachment from the surface

248 are depicted in Fig. 3. The coordination spheres will be referred as M-(O-Mg)$_n$ or M-(O-Si)$_m$

249 in the following (n and m standing for the number of Mg and Si neighbors, respectively).

250 Whereas the coordination of Si-(O-Si)$_m$ is dominated by a single mode for which $m = 1$,

251 others are more dispersed around one or more principal modes. Regarding Mg-(O-Mg)$_n$, n is

always an even number, regardless of the set of probabilities, consistent with the structure of

enstatite. The value of the principal modes of Mg-(O-Mg)$_n$, Mg-(O-Si)$_m$, and Si-(O-Mg)$_m$

depends on the probability and differs from one face to another, as illustrated in Fig. 3, where

the blue and red bars corresponds to two distinct sets of probabilities ([$P_{Mg-O-Mg}$ = 0.99, $P_{Mg-O-Si}$ = 0.3, $P_{Si-O-Si}$ = 0.0109] and [$P_{Mg-O-Mg}$ = 0.7, $P_{Mg-O-Si}$ = 0.3 and $P_{Si-O-Si}$ = 0.1547]) selected

from the slowest and fastest range of dissolution rates respectively. However, these

distributions also reveal that the mean coordination spheres remain constant, regardless of the

set of probabilities used to run the simulation or the face that is considered (4.02 ± 0.01; 6.64

± 0.02 and 1.002 ± 0.002 for Mg-O-Mg; Mg-O-Si+Mg-O-Si and Si-O-Si bonds, respectively).
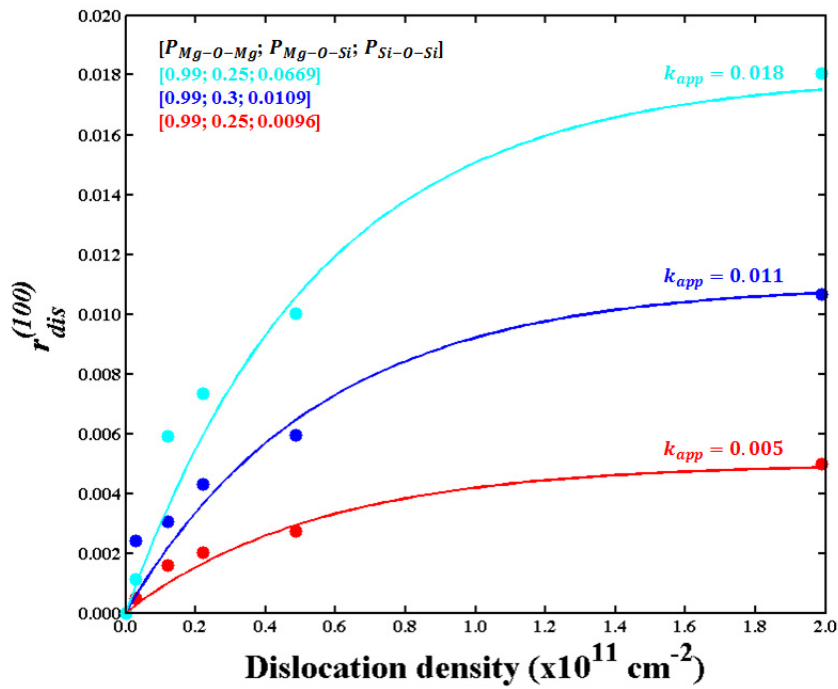
Fig 4. Contribution of dissolution rate specific to dislocations ($r^{(100)}_{dislocation}$) to the total dissolution rate ($r^{(100)}_{\square}$) as a function of the dislocation density. The filled circles represent the results of the different simulations and lines, the application of Eq. 16 using the parameters that allow for the best fit of all the simulations. Colors represent different [$P_{Mg-O-Mg}$; $P_{Mg-O-Si}$; $P_{Si-O-Si}$] input probabilities: [0.99; 0.25; 0.0669], [0.99; 0.3; 0.0109] and [0.99; 0.25; 0.0096] for the cyan, blue and red lines respectively. Values of k_{app} are 0.018, 0.011 and 0.005 for the cyan, blue and red lines respectively.

261

262   *3.3. Dislocation density*

263   The results of simulations conducted with dislocations are reported in Fig. 4. The

264   dislocation density has been investigated by varying the surface area (i.e., all simulations were

265   conducted using a single dislocation line, while varying the simulated surface area).

266   Simulations containing dislocations have been conducted on the (100) face. The presented

267   result show the relation between the dissolution rate and the dislocation density after

268   subtraction of the "bulk" contribution to the overall dissolution rate (i.e., $r_{dislocation}^{(hkl)} = r^{(hkl)} -$

269    $r_{bulk}^{(hkl)}$). The results highlight an asymptotic relationship between dissolution rate and

270   dislocation density.

271

272   4. Discussion

273   *4.1 Bulk dissolution rate evolution as a function of bond-breaking probabilities*

274   From the numerical experiments described in Section 3.1, the steady state dissolution

275   rates of enstatite (defined as congruent and constant dissolution rates with time) are

276   proportional to each individual bond-breaking probability raised at a given power inferred

277   from the linear regressions depicted in a log-log diagram (Fig. 2). Moreover, since the slope

278   of the linear regression between Log(P_i) (*i* stands for Mg-O-Mg or Mg-O-Si or Si-O-Si) and

279   Log(*r*) is constant whatever the difference between the two other involved probabilities; a

280   more general function of the dissolution rate can be written as:

$$r_{bulk}^{(hkl)} = k\, P_{Mg-O-Mg}^{\alpha}\, P_{Mg-O-Si}^{\beta}\, P_{Si-O-Si}^{\gamma} \tag{5}$$

281   where *k* is a constant and α, β, γ are the corresponding slopes listed in Table 2 for the various

282   regressions. The parameter *k* is then obtained using equation 5 and is constant for each face.

283   The different parameter values are summarized in Table 2, the α, β, γ values are obtained by

284 taking the average values of the corresponding slopes and the dissolution rates calculated with

285 the surrogate model (Eq. 5) are compared with the simulated one in Fig. 5.

Face	k	α	β	γ
(100)	8.87	2.46	4.62	0.94
(010)	7.80	2.22	4.65	0.75
(001)	4.72	6.36	4.19	0.14

286 **Table 2.** Values of the different face-specific parameters of the surrogate model.

287

288 If the parameter α can be considered as constant for (100) and (010) faces (Table 1), the slope

289 that corresponds to a variation of $P_{Mg-O-Mg}$ decreases from 7.46 to 5.05 when the difference

290 between $E_{Mg-O-Si}$ and $E_{Si-O-Si}$ decreases, i.e., when $E_{Mg-O-Si}$ gets closer to $E_{Si-O-Si}$. For these

291 cases, the assumptions used in the concept of the surrogate model may not be fulfilled (e.g., k

292 is constant and does not depend on the different probabilities). This assumption will be

293 discussed in the next section. Despite this approximation and the apparent trend for the (001)

294 face, the proposed model described by Eq. 5 is capable of satisfactorily estimating the

295 simulated dissolution rates (Fig. 5) for the three different faces. Note that Eq. (5) has been

296 derived from simulations where only the first coordination sphere of surface atoms is

297 considered for expressing the dissolution probability of individual atoms. Several studies [36, 64]

298 have shown that second coordination sphere may also play a role in the dissolution, and may

299 impact the shape of the developed etch pits. However, we showed that considering only the

300 first coordination sphere is enough to reproduce satisfactorily the face-specific shape of etch

301 pits observed on enstatite [41], explaining why we stick to this model in the present study.

302 Considering the impact of the second coordination sphere would make Eq. 5 more

303 sophisticated, since it would probably incorporate specific terms related to the second

304 coordination spheres.

4.2. Theoretical interpretation of the surrogate model

The development of the surrogate expression given in Eq. 5 is derived from a statistical analysis of the outputs of the stochastic simulations of enstatite dissolution, with no preconception of the mathematical form that should be used to relate the steady-state dissolution rates to the individual bond-breaking probabilities describing enstatite hydrolysis. In the present section, we provide a possible theoretical explanation of Eq. 5.

The dissolution rate can be defined as the derivative of the number of atoms that are dissolved with time:

$$r = \frac{dN_{M,d}}{dt} \tag{6}$$

where $N_{M,d}$ stands for the amount of dissolved atoms belonging to the M species during the time interval dt. Arguably, $N_{M,d}$ should depend on two parameters: the amount of atoms located at the mineral surface ($N_{M,S}$) and the intrinsic detachment rate of these atoms. Importantly, classical theories of dissolution kinetics suggest that at steady-state conditions, $N_{M,S}$ is constant and proportional to the considered surface area [6]. This aspect was numerically verified in our previous study [41] where we showed that the amount of surface atoms level to a plateau as soon as the dissolution becomes congruent and the dissolution rate is constant. At steady state, the number of dissolved atoms of Mg or Si is given by:

$$N = \hat{N}_{Mg} P_{Mg} = \hat{N}_{Si} P_{Si} \tag{7}$$

where N is the number of dissolved atoms of Mg or Si, $\hat{N}_A$ is the number of atoms A (Mg or Si) at the mineral surface, P_A is the probability that atom A is dissolved. Following the previous equation, N can be rewritten as:

$$N = \sqrt{\hat{N}_{Mg} P_{Mg} \hat{N}_{Si} P_{Si}} \tag{8}$$
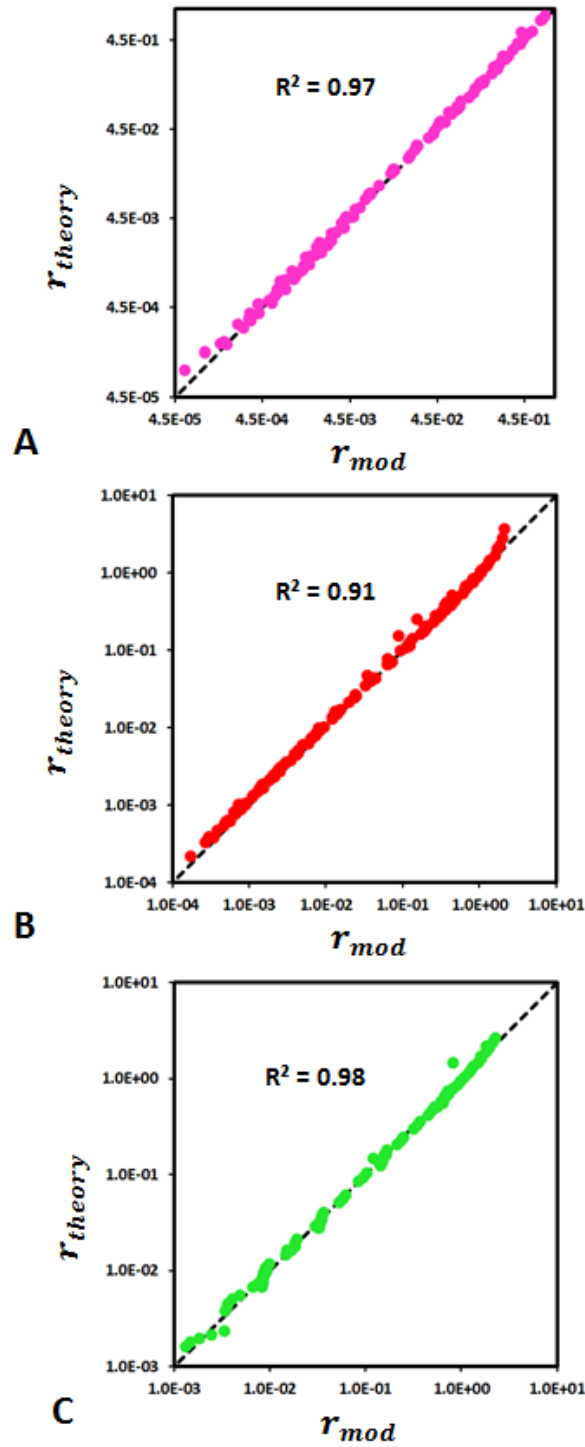
Fig 5. Comparison between the dissolution rates estimated with the surrogate model (r_{theory}; Eq. 5) and dissolution rates provided by the numerical simulations (r_{mod}) for faces (100) (A), (010) (B) and (001) (C). The comparison is made for all the different simulations listed in Table 1. For instance, (A) presents all the simulations shown in Fig. 2, and the rate variability results from the corresponding bond-breaking probabilities that are reported in Table 1.

324   The dissolution of an A atom for a given coordination sphere *i* is given by:

$$P_{A,i} = P_{A-A}^{\alpha_i} P_{A-B}^{\beta_i} \qquad (9)$$

25

where α_i and β_i are the number of bonds connecting the considered A atom to another A or to a B atom (Si or Mg accordingly), respectively. At the solid surface, we consider that there are N_C different coordination spheres and n_i atoms with a coordination sphere i. Therefore, the probability to dissolve the atom A over the mineral face is:

$$P_A = \frac{1}{\hat{N}_A} \sum_{i=1}^{N_C} n_i P_{A-A}^{\alpha_i} P_{A-B}^{\beta_i} \text{ and } \hat{N}_A = \sum_{i=1}^{N_C} n_i \tag{10}$$

Or

$$P_A = \frac{1}{\hat{N}_A} \left(\sum_{i=1}^{N_C} n_i P_{A-A}^{\alpha_i - \alpha_A} P_{A-B}^{\beta_i - \beta_A} \right) P_{A-A}^{\alpha_A} P_{A-B}^{\beta_A} = k_A P_{A-A}^{\alpha_A} P_{A-B}^{\beta_A} \tag{11}$$

with

$$k_A = \frac{1}{\hat{N}_A} \sum_{i=1}^{N_C} n_i P_{A-A}^{\alpha_i - \alpha_A} P_{A-B}^{\beta_i - \beta_A} \tag{12}$$

and the number of dissolved atoms is:

$$
\begin{aligned}
N &= \sqrt{\hat{N}_{Mg} \hat{N}_{Si}} \sqrt{k_{Mg} P_{MgOMg}^{\alpha_{Mg}} P_{MgOSi}^{\beta_{Mg}} k_{Si} P_{SiOSi}^{\alpha_{Si}} P_{MgOSi}^{\beta_{Si}}} \\
&= \sqrt{\hat{N}_{Mg} k_{Mg} \hat{N}_{Si} k_{Si}} P_{MgOMg}^{\alpha} P_{MgOSi}^{\beta} P_{SiOSi}^{\gamma}
\end{aligned}
\tag{13}
$$

with $\alpha = \alpha_{Mg}$, $\beta = \beta_{Mg} + \beta_{Si}$, $\gamma = \alpha_{Si}$.

The statistical analysis of the numerical experiments provides some values of the parameters k, α, β, γ (see Table 2). Surprisingly, the parameter k does not depend on the probabilities P_{A-A} and P_{A-B} in the range of the numerical values used for the experiments. An appropriate choice of (α_A, β_A) may explain this property. Assuming that $\alpha_A = \alpha_j$ and $\beta_A = \beta_j$, the constant k_A can be rewritten as:

$$k_A = \frac{n_j}{\hat{N}_A} + \frac{1}{\hat{N}_A} \sum_{i=1, i \neq j}^{N_C} n_i P_{A-A}^{\alpha_i - \alpha_j} P_{A-B}^{\beta_i - \beta_j} \tag{14}$$

338 Therefore, k_A can be a constant value if $n_j \gg \sum\limits_{i=1, i \neq j}^{N_C} n_i P_{A-A}^{\alpha_i - \alpha_j} P_{A-B}^{\beta_i - \beta_j}$ which is possible when

339 $\alpha_i > \alpha_j$ and/or $\beta_i > \beta_j$, for having positive exponents for the probabilities P_{A-A} and/or P_{A-B}.

340 Given that the exponents are positive, considering k as a constant is a reasonable assumption

341 if the difference between P_{A-A} and P_{A-B} is significant. The validity of this condition is

342 difficult to appreciate if P_{A-A} and P_{A-B} are close, as it is the case for the simulations run for

343 (001) face (see section 4.1 and Table 1). Finally, this demonstrates that the dissolution rate is

344 therefore compatible with Eq. 5:

$$r = W \frac{N}{dt} = W \frac{k P_{Mg-O-Mg}^{\alpha} P_{Mg-O-Si}^{\beta} P_{Si-O-Si}^{\gamma}}{dt} \text{ with } W = \frac{V_{cell}}{iter \times N_{cmx} \times S} \tag{15}$$

345 with N_{cmx} standing for the number of "complexes" (see 4.4) in the enstatite cell.

346

4.3. Accounting for the impact of dislocation density on the dissolution rates

348 Dislocations have a measurable impact on the dissolution rate, whatever the set of

349 probabilities that was tested (Fig 6C). This result is consistent with numerical and

350 experimental studies that showed that the presence of dislocations outcropping at mineral

351 surfaces globally increases the dissolution rate when the nucleation of etch pits is

352 thermodynamically favorable (i.e., at far-from-equilibrium conditions [11, 14, 16, 23, 31, 37]).

353 However, when dealing with natural samples, the dislocation density remains a parameter

354 impossible or difficult to control *a priori*, which complicates the prediction of its impact on

355 dissolution rate. Furthermore, several studies showed that the mineral dissolution rate is not a

356 strictly increasing function of the dislocation density [31, 37, 80] since above a given threshold, the

357 dissolution rate no longer varies with the dislocation density.

358 To qualitatively comply with the above-mentioned studies, the results for the (100)

359 face (Fig. 4) were fitted using the following empirical relation between dislocation density

360   and the additional dissolution rate resulting from etch pit opening at dislocation outcrop (see

361   Section 3.3.), which verifies that the dissolution rate levels to a plateau value when the

362   dislocation density tends towards infinity:

$$r_{dislocation}^{(100)} = k_{app}\left(1 - e^{-\frac{\rho_d}{\omega}}\right) \tag{16}$$

363   where k_{app} and ω ($\approx 5.51 \times 10^{10}$) are empirical parameters that were obtained by calibration

364   on the outputs of the simulations, and ρ_d is the dislocation density. Whereas ω does not seem

365   to vary with the probabilities used as input parameters, it clearly appears that k_{app} (Fig. 4)

366   depends on the individual bond-breaking probabilities. From a physical standpoint, this

367   observation may result from the fact the first coordination spheres of atoms in the vicinity of a

368   dislocation line differ from those of atoms considered for defect-free surface.

369   Considering this apparent relationship between k_{app} and the probabilities, a first

370   tentative to link the global rate to the probabilities and the dislocation density was performed

371   using the same exponent for each probability as the "bulk" case. Since the global rate is

372   equivalent to $r^{(hkl)} = r_{dislocation}^{(hkl)} + r_{bulk}^{(hkl)}$, it is possible to assume the following relation:

$$r^{(hkl)} = \left[k + k_{dis}\left(1 - e^{-\frac{\rho_d}{\omega}}\right)\right]P_{Mg-O-Mg}^{\alpha}P_{Mg-O-Si}^{\beta}P_{Si-O-Si}^{\gamma} \tag{17}$$

373   A comparison between this relation and the experimental results is given in Fig. 6A and the

374   value of k_{dis} is given in Table 3. Although the relationship between the surrogate model and

375   the results of the simulations was proven efficient to simulate the dissolution of defect-free

376   surfaces ($R^2 > 0.9$ in all cases), it is not the case when using Eq. 17, for which $R^2 = 0.76$.

377   In order to improve the agreement between the surrogate model of the global rate and

378   the results of the simulations, numerical experiments were run for face (100) with dislocations

379   similarly to Section 4.1. The dissolution rates were fitted using the following function:

$$r_{dislocation}^{(hkl)} = k_{dis} k\, P_{Mg-O-Mg}^{\alpha_{dis}} P_{Mg-O-Si}^{\beta_{dis}} P_{Si-O-Si}^{\gamma_{dis}} \left(1 - e^{-\frac{\rho_d}{\omega}}\right) \qquad (18)$$

The values of $\alpha_{dis}, \beta_{dis}, \gamma_{dis}$ are lower than those obtained in the "bulk" (defect-free) case (Table 3), which makes sense since the coordination spheres of atoms are arguably lower in the vicinity of the dislocation line, resulting in greater measured dissolution rates.

k_{dis}	α_{dis}	β_{dis}	$\gamma_{dis}\,\gamma$	R^2
227.9	**2.46**	**4.62**	**0.94**	0.72
44.7	2.09	4.09	0.67	0.86

Table 3. Values of the parameters of the model described by Eq. 17 and Eq. 18 and the correlation coefficient R^2. The bold characters represent the fitted parameters.

The global dissolution rate of enstatite can then be calculated by summing $r_{bulk}^{(hkl)}$ and $r_{dislocation}^{(hkl)}$, resulting in the following relation:

$$r^{(hkl)} = k P_{Mg-O-Mg}^{\alpha} P_{Mg-O-Si}^{\beta} P_{Si-O-Si}^{\gamma} + k_{dis} P_{Mg-O-Mg}^{\alpha_{dis}} P_{Mg-O-Si}^{\beta_{dis}} P_{Si-O-Si}^{\gamma_{dis}} \left(1 - e^{-\frac{\rho_d}{\omega}}\right) \qquad (19)$$

Therefore, the agreement between the results of the simulations and the surrogate model is improved and its correlation coefficient increases from 0.72 to 0.86 (Fig. 6B).

If this type of relations can be extended to other minerals and other types of defects (e.g. vacancies), they may represent an interesting method to link together dissolution rates derived from considerations at the atomic scale and those derived from observations at the mineral scale. This type of relations can also represent a significant progress for reactive transport models that simulate steady-state dissolution reactions. Indeed, even though the present work represents a preliminary step to link relations at the atomic scale to macroscopic dissolution rates, it shows promise as a mean to express face-specific steady-state dissolution rates as a function of the bond-breaking probabilities (and therefore, of the activation energies of hydrolysis) of the different types of bonds that exist for a given mineral. While some studies have questioned the possibility to use the outputs of Monte Carlo simulations in

401 reactive-transport codes because of the limited space- and time-scales investigated following

402 such stochastic treatments of the dissolution process, here we show that steady-state

403 dissolution rates may be satisfactorily calculated from considerations at the atomic scale. As a

404 consequence, rate equations similar to Eq. 17 or Eq. 19 may be simply implemented in

405 reactive transport codes as the rate-constant of the source term of the classical reaction-

406 advection-diffusion equation. This may be of interest for modeling processes for which the

407 fluid composition can be considered as unchanged over the considered simulated time, such

408 as chemical weathering in rivers or in some aquifers with a constant fluid velocity, or fluid

409 circulation in deep fractured geothermal reservoirs, where the fluid composition is

410 approximately constant and poorly affected by geothermal power plant functioning (e.g. [81]).

411 More work remains however needed to assess whether this result is limited to enstatite or the
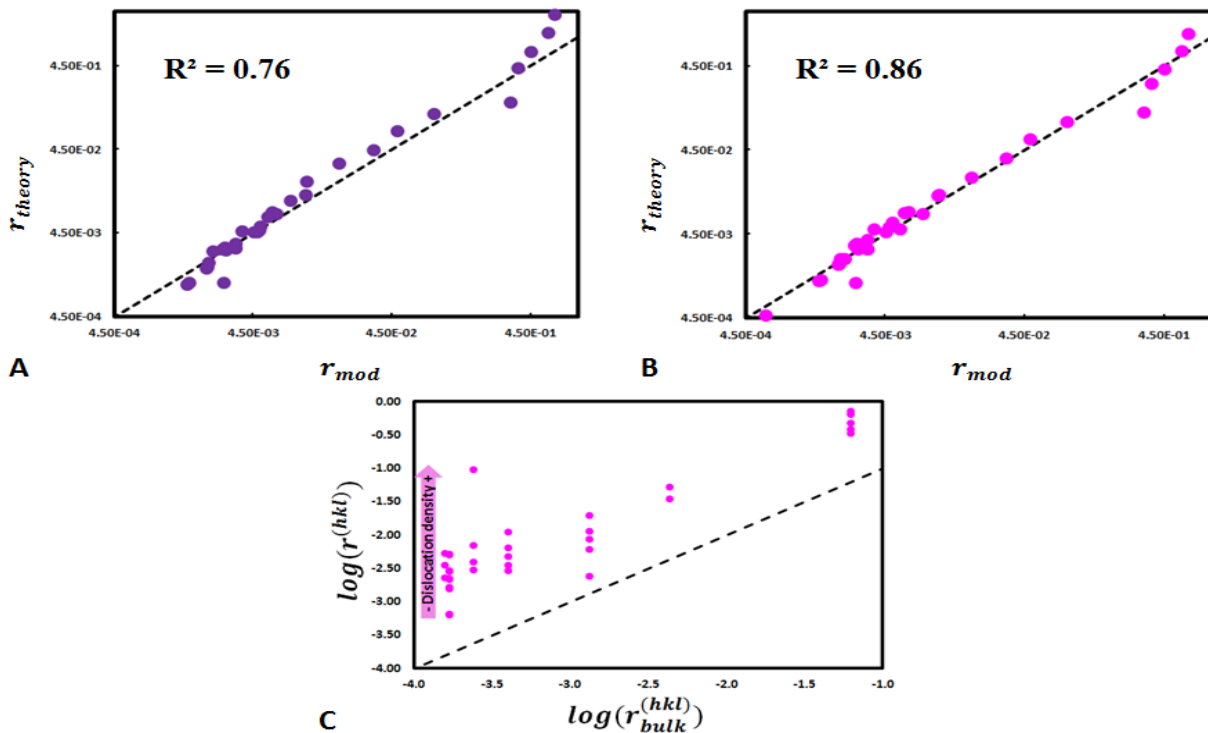
Figure 6. Comparison of experimental dissolution rates (r_{mod}) and dissolution rates determined with the surrogate model (r_{theory}) with the presence of one dislocation (dislocation density is changed by varying the surface area). Agreement using (A) Eq. 17 and (B) Eq. 19. (C) Comparison between dislocation-driven dissolution and bulk (dislocation-free) dissolution. The presence of dislocations increases dissolution rates for all the simulations. The data points represent the simulations conducted using sets of probabilities and dislocation densities given in Table 4.

412   pyroxene group (there is a priori no reason to think so), as well as expanding the relation to

413   the transient regime, where the dissolution rate is neither stoichiometric nor constant. As long

414   as this latter task remains not fulfilled, alternate approaches such as the use of Voronoi

415   distance maps [39, 73] probably represents the most promising compromise to upscale kinetic

416   Monte Carlo simulations. This strategy nonetheless remains far more complicated than just

417   using a surrogate expression as proposed above.

Dislocation density	MgOMg	MgOSi	SiOSi
1.99E+11	**0.99**	**0.3**	**0.0109**
1.99E+11	**0.99**	**0.25**	**0.0096**
1.99E+11	0.99	0.9	0.0096
1.99E+11	**0.99**	**0.25**	**0.0091**
1.99E+11	0.99	0.25	0.0669
4.88E+10	**0.99**	**0.3**	**0.0109**
4.88E+10	**0.99**	**0.25**	**0.0096**
4.88E+10	0.99	0.9	0.0096
4.88E+10	**0.99**	**0.25**	**0.0091**
4.88E+10	0.99	0.25	0.0669
2.21E+10	**0.99**	**0.3**	**0.0109**
2.21E+10	**0.99**	**0.25**	**0.0096**
2.21E+10	0.99	0.9	0.0096
2.21E+10	**0.99**	**0.25**	**0.0091**
2.21E+10	0.99	0.25	0.0669
1.21E+10	**0.99**	**0.3**	**0.0109**
1.21E+10	**0.99**	**0.25**	**0.0096**
1.21E+10	0.99	0.9	0.0096
1.21E+10	**0.99**	**0.25**	**0.0091**
1.21E+10	0.99	0.25	0.0669
3.00E+09	**0.99**	**0.3**	**0.0109**
3.00E+09	**0.99**	**0.25**	**0.0096**
3.00E+09	0.99	0.9	0.0096
3.00E+09	**0.99**	**0.25**	**0.0091**
3.00E+09	0.99	0.25	0.0669
1.9899E+11	0.99	0.5	0.0096
1.9899E+11	0.8	0.3	0.0109
1.9899E+11	0.7	0.3	0.0109
4.8773E+10	0.99	0.5	0.0096
4.8773E+10	0.8	0.3	0.0109
4.8773E+10	0.7	0.3	0.0109
2.211E+10	0.99	0.5	0.0096
2.211E+10	0.8	0.3	0.0109
2.211E+10	0.7	0.3	0.0109

418

419 **Table 4.** Dislocation densities and probabilities used in the simulations used for Fig. 5. Bolded lines represent
420 the input parameters used in the simulations shown in Fig. 3.

421

422 ***4.4. Relation between the coordination of atoms leaving the surface and the***
423 ***surrogate expression***

424 Interestingly, when atoms are released from the mineral surface, they seem to have a

425 specific average coordination. This assertion is supported by the analysis of the environment

426 of Mg and Si when they leave the surface, since the mean values of Mg-O-Mg, Mg-O-Si+Mg-

427 O-Si and Si-O-Si bonds remain constant and unaffected by the set of probabilities used to run

428 the simulations for all faces (see Section 3.2). However, the numerical values of the

429 parameters used in the surrogate expression of the dissolution rate are face-specific. This

430 apparent paradox can be easily explained by recalling that the histograms reported in Fig. 3

431 actually take into account all atoms leaving the surface, including those whose departure is

432 not rate-limiting of the dissolution process.

433 By analogy with Eq. 3, the surrogate expression given by Eq. 17 or Eq. 19 may reflect

434 the average coordination of atoms that control the dissolution process, as kink sites would do.

435 The fact that the numerical values of α, β and γ are face-specific indicates that this average

436 rate-controlling configuration is not unique for a given mineral. Most likely, this result

437 reflects the fact that kink sites, which are much more difficult to define using a real crystal

438 lattice than simplified isotropic cubic Kossel crystals, differ from one face to another when

439 dealing with anisotropic structures. This explanation would in turn be consistent with the

440 observed anisotropic reactivity of the pyroxene structure.

441

442 # 5. Conclusion

443 In this study, we presented the results of hundreds of probabilistic simulations of

444 enstatite dissolution to link the overall dissolution rate to the bond-breaking probabilities used

as input parameters. By varying independently each probability, we showed that it is possible to build a surrogate model that links the different probabilities to the dissolution rate following a power law. This result contributes to the general effort of upscaling of mineral dissolution kinetics, since this surrogate expression is based on a mechanistic approach developed from considerations at the atomic-scale, from which the resulting dissolution rate constants can be used as a source term in reactive transport simulations. However, the relation remains valid at steady-state conditions only, and the transient regime must be treated following other upscaling approaches, such as the use of Voronoï distance maps [39, 73].

The various simulations conducted with dislocations have shown that it is possible to link the dissolution rate to the dislocation density by introducing an exponential factor to the global $r = f\left(\prod_i P_i^{z_i}\right)$ relation. This relation further extends the interest of probabilistic simulations of mineral dissolution to account for the impact of some important parameters that are hardly controlled in experimental studies. In addition, in case of a bond hydrolysis with significant higher activation energy than the others, the dissolution rate is strongly correlated to this activation energy, and the surrogate model may be used to estimate the value of this parameter.

However, the surrogate model also presents some limitations, particularly when M-O-Si and Si-O-Si hydrolysis probabilities are getting close to each other (where M is a divalent cation, i.e., Mg in the case of enstatite). In this specific case, the results may be out of the limits of the theoretical framework that supports the development of the surrogate expression. Of note, such cases are however those for which the input parameters are physically unrealistic, as the activation energy of Si-O-Si hydrolysis is admitted to be much lower than any other M-O-Si bond.

468　　　　Finally, this study represents a first step towards the development of surrogate

469　expressions of mineral dissolution rates. Its application to natural environment, its extension

470　to other groups of minerals as well as its extension to transient state still have to be explored.

471

6. Acknowledgements

476

7. References

478　1.　　Berner, R. A.; Lasaga, A. C.; Garrels, R. M., The Carbonate-Silicate Cycle and Its Effect on
479　Atmospheric Carbon Dioxide over the Past 100 Millions Years. *Am J Sci* **1983**, *284*, 641-683.
480　2.　　Berner, R. A., A Model for Atmospheric Co2 over Phanerozoic Time. *Am J Sci* **1991**, *291*,
481　339-376.
482　3.　　Berner, R. A., 3GEOCARB-II - a Revised Model of Atmospheric Co2 over Phanerozoic Time.
483　*Am J Sci* **1994**, *294*, 56-91.
484　4.　　Berner, R. A.; Kothavala, Z., GEOCARB III: A Revised Model of Atmospheric Co2 over
485　Phanerozoic Time. *Am J Sci* **2001**, *301*, 182-204.
486　5.　　Lasaga, A. C., Transition State Theory. In *Kinetics of Geochemical Process*, Lasaga, A. C.,
487　and Kirkpatrick, R.J, Ed. Mineralogical Society of America: 1981; Vol. 8, pp 135-169.
488　6.　　Aagaard, P.; Helgeson, H. C., Thermodynamic and Kinetic Constraints on Reaction-Rates
489　among Minerals and Aqueous-Solutions .1. Theoretical Considerations. *Am J Sci* **1982**, *282*, 237-285.
490　7.　　Oelkers, E. H.; Schott, J.; Devidal, J.-L., The Effect of Aluminum, Ph, and Chemical Affinity
491　on the Rates of Aluminosilicate Dissolution Reactions. *Geochim Cosmochim Ac* **1994**, *58*, 2011-2024.
492　8.　　Lasaga, A. C., Fundamental Approaches in Describing Mineral Dissolution and Precipitation
493　Rates. In *Chemical Weathering Rates of Silicate Minerals*, White, A. F.; Brantley, S. L., Eds.
494　Mineralogical Society of America: 1995; Vol. 31, pp 23-86.
495　9.　　Gin, S.; Jegou, C.; Frugier, P.; Minet, Y., Theoretical Consideration on the Application of the
496　Aagaard-Helgeson Rate Law to the Dissolution of Silicate Minerals and Glasses. *Chem Geol* **2008**,
497　*255*, 14-24.
498　10.　　Luttge, A., Crystal Dissolution Kinetics and Gibbs Free Energy. *Journal of Electron
499　Spectroscopy and Related Phenomena* **2006**, *150*, 248-259.
500　11.　　Burch, T. E.; Nagy, K. L.; Lasaga, A. C., Free Energydependence of Albite Dissolution
501　Kinetics at 80°C and Ph 8.8. *Chem Geol* **1993**, *105*, 137-162.
502　12.　　Taylor, A. S.; Blum, J. D.; Lasaga, A. C., The Dependence of Labradorite Dissolution and Sr
503　Isotope Release Rates on Solution Saturation State. *Geochim Cosmochim Ac* **2000**, *64*, 2389-2400.
504　13.　　Beig, M. S.; Luttge, A., Albite Dissolution Kinetics as a Function of Distance from
505　Equilibrium: Implications for Natural Feldspar Weathering. *Geochim Cosmochim Ac* **2006**, *70*, 1402-
506　1420.

14. Hellmann, R.; Tisserand, D., Dissolution Kinetics as a Function of the Gibbs Free Energy of Reaction: An Experimental Study Based on Albite Feldspar. *Geochim Cosmochim Ac* **2006**, *70*, 364-383.

15. Dixit, S.; Carroll, S. A., Effect of Solution Saturation State and Temperature on Diopside Dissolution. *Geochemical Transactions* **2007**, *8*.

16. Arvidson, R. S.; Luttge, A., Mineral Dissolution Kinetics as a Function of Distance from Equilibrium - New Experimental Results. *Chem Geol* **2010**, *269*, 79-88.

17. Daval, D.; Hellmann, R.; Corvisier, J.; Tisserand, D.; Martinez, I.; Guyot, F., Dissolution Kinetics of Diopside as a Function of Solution Saturation State: Macroscopic Measurements and Implications for Modeling of Geological Storage of Co2. *Geochim Cosmochim Ac* **2010**, *74*, 2615-2633.

18. Nicoleau, L.; Nonat, A.; Perrey, D., The Di- and Tricalcium Silicate Dissolutions. *Cement and Concrete Research* **2013**, *47*, 14-30.

19. Pollet-Villard, M.; Daval, D.; Ackerer, P.; Saldi, G. D.; Wild, B.; Knauss, K. G.; Fritz, B., Does Crystallographic Anisotropy Prevent the Conventional Treatment of Aqueous Mineral Reactivity? A Case Study Based on K-Feldspar Dissolution Kinetics. *Geochim Cosmochim Ac* **2016**, *190*, 294-308.

20. Fischer, C.; Arvidson, R. S.; Lüttge, A., How Predictable Are Dissolution Rates of Crystalline Material? *Geochim Cosmochim Ac* **2012**, *98*, 177-185.

21. Godinho, J. R. A.; Piazolo, S.; Evins, L. Z., Effect of Surface Orientation on Dissolution Rates and Topography of Caf2. *Geochim Cosmochim Ac* **2012**, *86*, 392-403.

22. Daval, D.; Hellmann, R.; Saldi, G. D.; Wirth, R.; Knauss, K. G., Linking Nm-Scale Measurements of the Anisotropy of Silicate Surface Reactivity to Macroscopic Dissolution Rate Laws: New Insights Based on Diopside. *Geochim Cosmochim Ac* **2013**, *107*, 121-134.

23. Smith, M. E.; Knauss, K. G.; Higgins, S. R., Effects of Crystal Orientation on the Dissolution of Calcite by Chemical and Microscopic Analysis. *Chem Geol* **2013**, *360–361*, 10-21.

24. Wild, B.; Daval, D.; Guyot, F.; Knauss, K. G.; Pollet-Villard, M.; Imfeld, G., Ph-Dependent Control of Feldspar Dissolution Rate by Altered Surface Layers. *Chem Geol* **2016**, *442*, 148-159.

25. Kurganskaya, I.; Luttge, A., Kinetic Monte Carlo Approach to Study Carbonate Dissolution. *The Journal of Physical Chemistry C* **2016**, *120*, 6482-6492.

26. Daval, D.; Bernard, S.; Rémusat, L.; Wild, B.; Guyot, F.; Micha, J. S.; Rieutord, F.; Magnin, V.; Fernandez-Martinez, A., Dynamics of Altered Surface Layer Formation on Dissolving Silicates. *Geochim Cosmochim Ac* **2017**, *209*, 51-69.

27. Fischer, C.; Luttge, A., Pulsating Dissolution of Crystalline Matter. *Proceedings of the National Academy of Sciences* **2018**, *115*, 897-902.

28. Zhang, L.; Lüttge, A., Aluminosilicate Dissolution Kinetics: A General Stochastic Model. *The Journal of Physical Chemistry B* **2008**, *112*, 1736-1742.

29. Brantley, S. L.; Crane, S. R.; Crerar, D. A.; Hellmann, R.; Stallard, R., Dissolution at Dislocation Etch Pits in Quartz. *Geochim Cosmochim Ac* **1986**, *50*, 2349-2361.

30. Lasaga, A. C.; Blum, A. E., Surface Chemistry, Etch Pits and Mineral-Water Reactions. *Geochim Cosmochim Ac* **1986**, *50*, 2363-2379.

31. Lasaga, A. C.; Luttge, A., Variation of Crystal Dissolution Rate Based on a Dissolution Stepwave Model. *Science* **2001**, *291*, 2400-2404.

32. Bouissonnié, A.; Daval, D.; Marinoni, M.; Ackerer, P., From Mixed Flow Reactor to Column Experiments and Modeling: Upscaling of Calcite Dissolution Rate. *Chem Geol* **2018**, *487*, 63-75.

33. Amelinckx, S., The Direct Observation of Dislocations. *Solid State Physics* **1964**.

34. Teng, H. H., Controls by Saturation State on Etch Pit Formation During Calcite Dissolution. *Geochim Cosmochim Ac* **2004**, *68*, 253-262.

35. Kurganskaya, I.; Arvidson, R. S.; Fischer, C.; Luttge, A., Does the Stepwave Model Predict Mica Dissolution Kinetics? *Geochim Cosmochim Ac* **2012**, *97*, 120-130.

36. Kurganskaya, I.; Luttge, A., A Comprehensive Stochastic Model of Phyllosilicate Dissolution: Structure and Kinematics of Etch Pits Formed on Muscovite Basal Face. *Geochim Cosmochim Ac* **2013**, *120*, 545-560.

37. Pollet-Villard, M.; Daval, D.; Fritz, B.; Knauss, K. G.; Schäfer, G.; Ackerer, P., Influence of Etch Pit Development on the Surface Area and Dissolution Kinetics of the Orthoclase (001) Surface. *Chem Geol* **2016**, *447*, 79-92.

38. Perez, A.; Daval, D.; Fournier, M.; Vital, M.; Delaye, J.-M.; Gin, S., Comparing the Reactivity of Glasses with Their Crystalline Equivalents: The Case Study of Plagioclase Feldspar. *Geochim Cosmochim Ac* **2019**, *254*, 122-141.

39. Luttge, A.; Arvidson, R. S.; Fischer, C.; Kurganskaya, I., Kinetic Concepts for Quantitative Prediction of Fluid-Solid Interactions. *Chem Geol* **2019**, *504*, 216-235.

40. Trindade Pedrosa, E.; Kurganskaya, I.; Fischer, C.; Luttge, A., A Statistical Approach for Analysis of Dissolution Rates Including Surface Morphology. *Minerals* **2019**, *9*, 458.

41. Bouissonnié, A.; Daval, D.; Guyot, F.; Ackerer, P., The Dissolution Anisotropy of Pyroxenes: Experimental Validation of a Stochastic Dissolution Model Based on Enstatite Dissolution. *The Journal of Physical Chemistry C* **2020**, *124*, 3122-3140.

42. Schott, J.; Berner, R. A., X-Ray Photoelectron Studies of the Mechanism of Iron Silicate Dissolution During Weathering. *Geochim Cosmochim Ac* **1983**, *47*, 2233-2240.

43. Eggleston, C. M.; Hochella, M. F.; Parks, G. A., Sample Preparation and Aging Effects on the Dissolution Rate and Surface-Composition of Diopside. *Geochim Cosmochim Ac* **1989**, *53*, 797-804.

44. Gratz, A. J.; Manne, S.; Hansma, P. K., Atomic Force Microscopy of Atomic-Scale Ledges and Etch Pits Formed During Dissolution of Quartz. *Science* **1991**, *251*, 1343-1346.

45. Jordan, G.; Rammensee, W., Dissolution Rates and Activation Energy for Dissolution of Brucite (001) : A New Method Based on the Microtopography of Crystal Surfaces. *Geochim Cosmochim Ac* **1996**, *60*, 5055-5062.

46. Lüttge, A.; Bolton, E. W.; Lasaga, A. C., An Interferometric Study of the Dissolution Kinetics of Anorthite; the Role of Reactive Surface Area. *Am J Sci* **1999**, *299*, 652-678.

47. Wirth, R., Focused Ion Beam (Fib): A Novel Technology for Advanced Application of Micro- and Nanoanalysis in Geosciences and Applied Mineralogy. *Eur J Mineral* **2004**, *16*, 863-876.

48. Cailleteau, C.; Angeli, F.; Devreux, F.; Gin, S.; Jestin, J.; Jollivet, P.; Spalla, O., Insight into Silicate-Glass Corrosion Mechanisms. *Nature Materials* **2008**, *7*, 978-983.

49. Noiriel, C., Resolving Time-Dependent Evolution of Pore-Scale Structure, Permeability and Reactivity Using X-Ray Microtomography. *Reviews in Mineralogy and Geochemistry* **2015**, *80*, 247-285.

50. Hellmann, R.; Cotte, S.; Cadel, E.; Malladi, S.; Karlsson, L. S.; Lozano-Perez, S.; Cabié, M.; Seyeux, A., Nanometre-Scale Evidence for Interfacial Dissolution–Reprecipitation Control of Silicate Glass Corrosion. *Nat Mater* **2015**, *14*, 307-311.

51. Leonard, D. N.; Hellmann, R., Exploring Dynamic Surface Processes During Silicate Mineral (Wollastonite) Dissolution with Liquid Cell Tem. *Journal of microscopy* **2017**, *265*, 358-371.

52. Ruiz-Agudo, E.; King, H. E.; Patiño-López, L. D.; Putnis, C. V.; Geisler, T.; Rodriguez-Navarro, C.; Putnis, A., Control of Silicate Weathering by Interface-Coupled Dissolution-Precipitation Processes at the Mineral-Solution Interface. *Geology* **2016**, *44*, 567-570.

53. Geisler, T.; Dohmen, L.; Lenting, C.; Fritzsche, M. B. K., Real-Time in Situ Observations of Reaction and Transport Phenomena During Silicate Glass Corrosion by Fluid-Cell Raman Spectroscopy. *Nature Materials* **2019**, *18*, 342-348.

54. Xiao, Y.; Lasaga, A. C., Ab Initio Quantum Mechanical Studies of the Kinetics and Mechanisms of Silicate Dissolution: H+(H3o+) Catalysis. *Geochim Cosmochim Ac* **1994**, *58*, 5379-5400.

55. Pelmenschikov, A.; Strandh, H.; Pettersson, L. G.; Leszczynski, J., Lattice Resistance to Hydrolysis of Si− O− Si Bonds of Silicate Minerals: Ab Initio Calculations of a Single Water Attack onto the (001) and (111) B-Cristobalite Surfaces. *The Journal of Physical Chemistry B* **2000**, *104*, 5779-5783.

56. Criscenti, L. J.; Kubicki, J. D.; Brantley, S. L., Silicate Glass and Mineral Dissolution: Calculated Reaction Paths and Activation Energies for Hydrolysis of a Q(3) Si by H3o+ Using Ab Initio Methods. *Journal of Physical Chemistry A* **2006**, *110*, 198-206.

57. Morrow, C. P.; Nangia, S.; Garrison, B. J., Ab Initio Investigation of Dissolution Mechanisms in Aluminosilicate Minerals. *The Journal of Physical Chemistry A* **2009**, *113*, 1343-1352.

614 58. Morrow, C. P.; Kubicki, J. D.; Mueller, K. T.; Cole, D. R., Description of Mg2+ Release from
615 Forsterite Using Ab Initio Methods. *The Journal of Physical Chemistry C* **2010**, *114*, 5417-5428.
616 59. Morrow, C. P.; Olsen, A. A.; Kubicki, J. D., Quantum Mechanical Modeling of Hydrolysis
617 and H2o-Exchange in Mg-, Ca-, and Ni-Silicate Clusters: Implications for Dissolution Mechanisms of
618 Olivine Minerals. *Am Mineral* **2014**, *99*, 2303-2312.
619 60. Lasaga, A. C.; Luttge, A., Mineralogical Approaches to Fundamental Crystal Dissolution
620 Kinetics - Dissolution of an a(3)B Structure. *Eur J Mineral* **2004**, *16*, 713-729.
621 61. Devreux, F.; Ledieu, A.; Barboux, P.; Minet, Y., Leaching of Borosilicate Glasses. Ii. Model
622 and Monte-Carlo Simulations. *Journal of Non-Crystalline Solids* **2004**, *343*, 13-25.
623 62. Zhang, L.; Lüttge, A., Al, Si Order in Albite and Its Effect on Albite Dissolution Processes: A
624 Monte Carlo Study. *Am Mineral* **2007**, *92*, 1316-1324.
625 63. Meakin, P.; Rosso, K. M., Simple Kinetic Monte Carlo Models for Dissolution Pitting Induced
626 by Crystal Defects. *The Journal of Chemical Physics* **2008**, *129*, 204106.
627 64. Kurganskaya, I.; Luttge, A., Kinetic Monte Carlo Simulations of Silicate Dissolution: Model
628 Complexity and Parametrization. *The Journal of Physical Chemistry C* **2013**, *117*, 24894-24906.
629 65. Briese, L.; Arvidson, R. S.; Luttge, A., The Effect of Crystal Size Variation on the Rate of
630 Dissolution – a Kinetic Monte Carlo Study. *Geochim Cosmochim Ac* **2017**, *212*, 167-175.
631 66. de Assis, T. A.; Aarão Reis, F. D. A., Dissolution of Minerals with Rough Surfaces. *Geochim*
632 *Cosmochim Ac* **2018**, *228*, 27-41.
633 67. Lasaga, A. C.; Luttge, A., Mineralogical Approaches to Fundamental Crystal Dissolution
634 Kinetics. *Am Mineral* **2004**, *89*, 527-540.
635 68. Zhang, L.; Luttge, A., Morphological Evolution of Dissolving Feldspar Particles with
636 Anisotropic Surface Kinetics and Implications for Dissolution Rate Normalization and Grain Size
637 Dependence: A Kinetic Modeling Study. *Geochim Cosmochim Ac* **2009**, *73*, 6757-6770.
638 69. Suarez, D.; Wood, J., Short-and Long-Term Weathering Rates of a Feldspar Fraction Isolated
639 from an Arid Zone Soil. *Chem Geol* **1996**, *132*, 143-150.
640 70. Lüttge, A.; Arvidson, R. S.; Fischer, C., A Stochastic Treatment of Crystal Dissolution
641 Kinetics. *Elements* **2013**, *9*, 183-188.
642 71. Knauss, K. G.; Johnson, J. W.; Steefel, C. I., Evaluation of the Impact of Co2, Co-
643 Contaminant Gas, Aqueous Fluid and Reservoir Rock Interactions on the Geologic Sequestration of
644 Co2. *Chem Geol* **2005**, *217*, 339-350.
645 72. Godderis, Y.; Francois, L. M.; Probst, A.; Schott, J.; Moncoulon, D.; Labat, D.; Viville, D.,
646 Modelling Weathering Processes at the Catchment Scale: The Witch Numerical Model. *Geochim*
647 *Cosmochim Ac* **2006**, *70*, 1128-1147.
648 73. Rohlfs, R.; Fischer, C.; Kurganskaya, I.; Luttge, A., Crystal Dissolution Kinetics Studied by a
649 Combination of Monte Carlo and Voronoi Methods. *Minerals* **2018**, *8*, 133.
650 74. Hugh-Jones, D. A.; J., A. R., A Compressional Study of Mgsio3 Orthoenstatite up to 8.5 Gpa.
651 *Am Mineral* **1994**, *79*, 405-410.
652 75. Bortz, A. B.; Kalos, M. H.; Lebowitz, J. L., A New Algorithm for Monte Carlo Simulation of
653 Ising Spin Systems. *Journal of Computational Physics* **1975**, *17*, 10-18.
654 76. Skrotzki, W., Defect Structure and Deformation Mechanisms in Naturally Deformed Augite
655 and Enstatite. *Tectonophysics* **1994**, *229*, 43-68.
656 77. Fischer, C.; Luttge, A., Beyond the Conventional Understanding of Water–Rock Reactivity.
657 *Earth Planet Sc Lett* **2017**, *457*, 100-105.
658 78. Fischer, C.; Kurganskaya, I.; Luttge, A., Inherited Control of Crystal Surface Reactivity. *Appl*
659 *Geochem* **2018**, *91*, 140-148.
660 79. Noiriel, C.; Daval, D., Pore-Scale Geochemical Reactivity Associated with Co2 Storage: New
661 Frontiers at the Fluid–Solid Interface. *Accounts of Chemical Research* **2017**, *50*, 759-768.
662 80. Schott, J.; Brantley, S.; Crerar, D.; Guy, C.; Borcsik, M.; Willaime, C., Dissolution Kinetics of
663 Strained Calcite. *Geochim Cosmochim Ac* **1989**, *53*, 373-382.
664 81. Sanjuan, B.; Millot, R.; Dezayes, C.; Brach, M., Main Characteristics of the Deep Geothermal
665 Brine (5km) at Soultz-Sous-Forêts (France) Determined Using Geochemical and Tracer Test Data. *Cr*
666 *Geosci* **2010**, *342*, 546-559.
667
668

669

670

671

672

673

674

675

676

677

678

679

680

681

682

683

684

685 **TOC Graphic**

686